and 15° was observed among the four structures (Table 2). In the majority of these cases, the change in the χ_2 angle relative to the original design remained near the value of 25° observed in the initial BIF_1 structure. This result suggested that mutations to Ala^{79} and Trp^{123} have the desired effect of rotating ring B without affecting the absolute orientation of ring A. Unfortunately, substitution of Tyr^{123} with the beta-branched Val and the opposing Ala^{79} with Ser (BIF_1.1) had the effect of rotating ring B even farther out of plane (35°) than in the original structure (Fig. 3A). This undesired rotation was partially remedied in BIF_1.2 (Φ = 21°) (Fig. 3B) by substituting Ala^{79} with a bulkier Val residue and further corrected in BIF_1.3 and BIF_1.4 (Φ = 15° and 20°, respectively) (Fig. 3, C and D) by replacing the opposing Tyr^{123} with a smaller Ala residue and Ala^{79} with Ser (BIF_1.3) or Val (BIF_1.4). This analysis suggested that ring A could potentially be rotated into a coplanar geometry by further increasing the size of the amino acid at position 79 with an Ala^{79}Ile mutation while maintaining Phe^{42} and the Tyr^{123}Ala mutation. The additional methyl group of the isoleucine should force the side of ring A to rotate further in the desired direction.

We next generated the corresponding BIF_0 mutant (S^8A, I^{11}BiPhe, Y^{79}I, F^{81}W, K^{121}I, and F^{123}A), purified the protein, and solved its crystal structure to 2.05 Å resolution (Fig. 4). Analysis of the electron density showed that the two phenyl rings of BiPhe are coplanar, which matches the configuration of the TS for the bond rotation reaction. The structure of BIF_0 shows that, in addition to adding steric bulk beneath ring A, the V^{79}I mutation also forces the side chain of Phe^{77} to adopt a different rotamer than was observed in BIF_1.4, which has the effect of further rotating ring A into the plane of ring B (Fig. 4). The mutations introduced into BIF_0 do not appear to substantially affect the thermal stability of the protein. The melting temperature of this mutant, as determined by differential scanning calorimetry, was ~110°C, consistent with the 3D structure of BIF_0, which shows that the protein core is well packed.

We have shown by iterative computational design, mutagenesis, and protein structure determination that one can design a protein core that stabilizes a simple conformational transition state to such a degree that one can determine its 3D x-ray crystal structure. However, we should note that the biphenyl energy landscape corresponds to a substructure within the protein relative to the energetics of the global protein conformational ensemble. A similar strategy was recently employed to directly observe catalyst-substrate interactions through x-ray crystallographic analysis (*33*). The results described here may not be all that surprising given that enzymes typically stabilize a rate-limiting TS by 8 to 12 kcal/mol. Nonetheless, these experiments underscore the ability of proteins to fold into defined 3D structures in which van der Waals, hydrogen-bonding, and electrostatic interactions can be controlled with exquisite precision.

REFERENCES AND NOTES

1. T. S. Rose, M. J. Rosker, A. H. Zewail, *J. Chem. Phys.* **88**, 6672–6673 (1988).
2. J. C. Polanyi, A. H. Zewail, *Acc. Chem. Res.* **28**, 119–132 (1995).
3. R. Srinivasan, J. S. Feenstra, S. T. Park, S. Xu, A. H. Zewail, *Science* **307**, 558–563 (2005).
4. H. Ihee *et al.*, *Science* **291**, 458–462 (2001).
5. L. Pauling, *Chem. Eng. News* **24**, 1375–1377 (1946).
6. W. P. Jencks, *Catalysis in Chemistry and Enzymology* (Dover, Mineola, NY, 1987).
7. A. Tramontano, K. D. Janda, R. A. Lerner, *Science* **234**, 1566–1570 (1986).
8. S. J. Pollack, J. W. Jacobs, P. G. Schultz, *Science* **234**, 1570–1573 (1986).
9. P. G. Schultz, R. A. Lerner, *Science* **269**, 1835–1842 (1995).
10. S. Dwivedi, S. P. Kruparani, R. Sankaranarayanan, *Nat. Struct. Mol. Biol.* **12**, 556–557 (2005).
11. F. Ceccacci, G. Mancini, P. Mencarelli, C. Villani, *Tetrahedron Asymmetry* **14**, 3117–3122 (2003).
12. A. Almenningen *et al.*, *J. Mol. Struct.* **128**, 59–76 (1985).
13. J. E. Katon, E. R. Lippincott, *Spectrochimica Acta* **15**, 627–650 (1959).
14. L. A. Carreira, T. G. Towns, *J. Mol. Struct.* **41**, 1–9 (1977).
15. H. Suzuki, *Bull. Chem. Soc. Jpn.* **32**, 1340–1350 (1959).
16. O. Bastiansen, S. Samdal, *J. Mol. Struct.* **128**, 115–125 (1985).
17. J. Xie, W. Liu, P. G. Schultz, *Angew. Chem. Int. Ed.* **46**, 9239–9242 (2007).
18. L. Wang, A. Brock, B. Herberich, P. G. Schultz, *Science* **292**, 498–500 (2001).
19. J. K. Eloranta, *Zeitschrift Naturforschung Teil A* **27a**, 1652–1662 (1972).
20. Materials and methods are available as supplementary materials on *Science* Online.
21. A. Razvi, J. M. Scholtz, *Protein Sci.* **15**, 1569–1578 (2006).
22. J. D. Bloom, S. T. Labthavikul, C. R. Otey, F. H. Arnold, *Proc. Natl. Acad. Sci. U.S.A.* **103**, 5869–5874 (2006).
23. A. Zanghellini *et al.*, *Protein Sci.* **15**, 2785–2794 (2006).
24. G. B. McGaughey, M. Gagné, A. K. Rappé, *J. Biol. Chem.* **273**, 15458–15463 (1998).
25. S. M. Le Grand, K. M. Merz, *J. Comput. Chem.* **14**, 349–352 (1993).
26. B. Kuhlman, D. Baker, *Proc. Natl. Acad. Sci. U.S.A.* **97**, 10383–10388 (2000).
27. M. C. Lawrence, P. M. Colman, *J. Mol. Biol.* **234**, 946–950 (1993).
28. A. Chatterjee, M. J. Lajoie, H. Xiao, G. M. Church, P. G. Schultz, *ChemBioChem* **15**, 1782–1786 (2014).
29. L. J. Shimon *et al.*, *Structure* **5**, 381–390 (1997).
30. S. Dwivedi, S. P. Kruparani, R. Sankaranarayanan, *Acta Crystallogr. D Biol. Crystallogr.* **60**, 1662–1664 (2004).
31. Y. Tanaka *et al.*, *Proteins* **61**, 1127–1131 (2005).
32. M. S. Cosgrove *et al.*, *Biochemistry* **45**, 7511–7521 (2006).
33. S. Han, B. V. Le, H. S. Hajare, R. H. G. Baxter, S. J. Miller, *J. Org. Chem.* **79**, 8550–8556 (2014).

ACKNOWLEDGMENTS

The authors thank N. P. King and P.-S. Huang for helpful discussions. D.B and J.H.M. were supported by the Defense Threat Reduction Agency (HDTRA1-11-1-0041). J.H.M. was supported by National Institute of General Medical Science of the National Institutes of Health under award F32GM099210. P.G.S. acknowledges support by the National Institutes of Health under award 2 R01 GM097206-05. The content is solely the responsibility of the authors and does not represent the official views of the National Institutes of Health. Structures of BIF_1, BIF_1.1 to BIF_1.4, and BIF_0 have been deposited in the Protein Data Bank under accession numbers 4S02, 4S0J, 4S0L, 4S0I, 4S0K, and 4S03.

SUPPLEMENTARY MATERIALS

www.sciencemag.org/content/347/6224/863/suppl/DC1
Materials and Methods
Figs. S1 and S2
Tables S1 and S2
References (*34*–*42*)

6 November 2014; accepted 20 January 2015
10.1126/science.aaa2424

ANIMAL EVOLUTION

Cope's rule in the evolution of marine animals

Noel A. Heim,[1]* Matthew L. Knope,[1]† Ellen K. Schaal,[1]‡ Steve C. Wang,[2] Jonathan L. Payne[1]

Cope's rule proposes that animal lineages evolve toward larger body size over time. To test this hypothesis across all marine animals, we compiled a data set of body sizes for 17,208 genera of marine animals spanning the past 542 million years. Mean biovolume across genera has increased by a factor of 150 since the Cambrian, whereas minimum biovolume has decreased by less than a factor of 10, and maximum biovolume has increased by more than a factor of 100,000. Neutral drift from a small initial value cannot explain this pattern. Instead, most of the size increase reflects differential diversification across classes, indicating that the pattern does not reflect a simple scaling-up of widespread and persistent selection for larger size within populations.

Body size constrains key ecological and physiological traits such as generation time, fecundity, metabolic rate, population size, and home range size (*1*, *2*). Because of perceived advantages associated with larger size, there has long been speculation that animals tend to increase in size over evolutionary time (*3*–*8*), a pattern commonly referred to as Cope's rule. Fossil data support size increase in many cases (*6*, *9*–*15*), but numerous counterexamples also exist (*16*–*22*). Moreover, some instances of size increase could simply result from neutral drift away from an initially small size rather than requiring any active selection for size (*17*, *22*).

To determine whether animal sizes have increased since the start of the Cambrian [542 million

[1]Department of Geological and Environmental Sciences, Stanford University, 450 Serra Mall, Stanford, CA 94305, USA. [2]Department of Mathematics and Statistics, Swarthmore College, Swarthmore, PA 19081, USA.
***Corresponding author. E-mail: naheim@stanford.edu** †Present address: Department of Biology, Stanford University, Stanford, CA 94305, USA. ‡Present address: Department of Geology, Lawrence University, Appleton, WI 54911, USA.

years ago (Ma)] and, if so, whether the increase can be accounted for by neutral drift or requires active evolutionary processes, we compiled adult body size measurements for 17,208 genera of marine animals from the phyla Arthropoda, Brachiopoda, Chordata, Echinodermata, and Mollusca, with stratigraphic ranges in the fossil record resolved to stages, the finest temporal units in the global geologic time scale (*23*) (fig. S1A). These phyla together account for 74% of animal diversity in the fossil record (*24*), and our data set covers 75% of total known genus diversity in these phyla. We measured the three major body axes from published images of specimens (typically holotypes of the type species) (*23*) in order to estimate the size of each genus as a simple geometric solid or from known length:mass relationships (*23*). We used linear regressions of biovolume on maximum length for classes and phyla to estimate the biovolume of genera for which fewer than three major axes were illustrated (*23*) (fig. S2 and table S1).

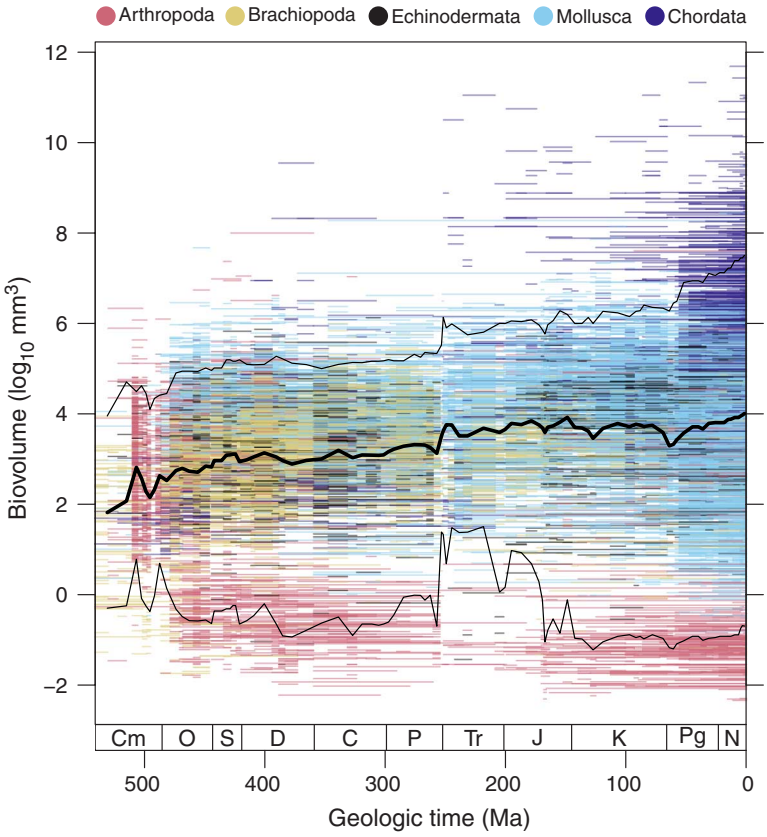

Fig. 1. Body size evolution across the past 542 million years. The distribution of fossil marine animal biovolumes across the Phanerozoic is shown. The colored horizontal lines show genus durations. The thick black line indicates the stage-level mean body size. The thin black lines demarcate the 5th and 95th percentiles. Cm, Cambrian; O, Ordovician; S, Silurian; D, Devonian; C, Carboniferous; P, Permian; Tr, Triassic; J, Jurassic; K, Cretaceous; Pg, Paleogene; N, Neogene.

Figure 1 illustrates the sizes of the marine animal genera in our data set across the past 542 million years. The mean biovolume across genera has increased by more than a factor of 150 (2.18 $\log_{10}$ units; the median increased by 2.35 $\log_{10}$ units) since the earliest Cambrian. Over the same interval, the range in biovolume expanded from 8 orders of magnitude in the Cambrian to 14 orders of magnitude in the Pleistocene (1 Ma). Most of this expansion in size range reflects an increase in the maximum, which climbed by more than three orders of magnitude between the Early Cambrian and Middle Devonian (542 to 385 Ma) and by an additional two orders of magnitude thereafter. In contrast, the overall minimum size decreased by less than one order of magnitude between the Early Cambrian and Middle Devonian and has remained stable ever since.

To test models of neutral change relative to active processes, we compared observed trends in maximum, mean, and minimum size to expectations generated by three evolutionary branching models: an unbiased random walk (i.e., Brownian motion; fig. S3A), a bounded random walk (i.e., Brownian motion with a reflecting lower bound; fig. S3B), and a size-biased random walk (fig. S3C) (*23*). The size-biased model fit observed trends in the minimum, mean, and maximum size better than the neutral and lower-bounded models (Fig. 2 and fig. S4). The observed minimum size is within the predicted range of all three models,

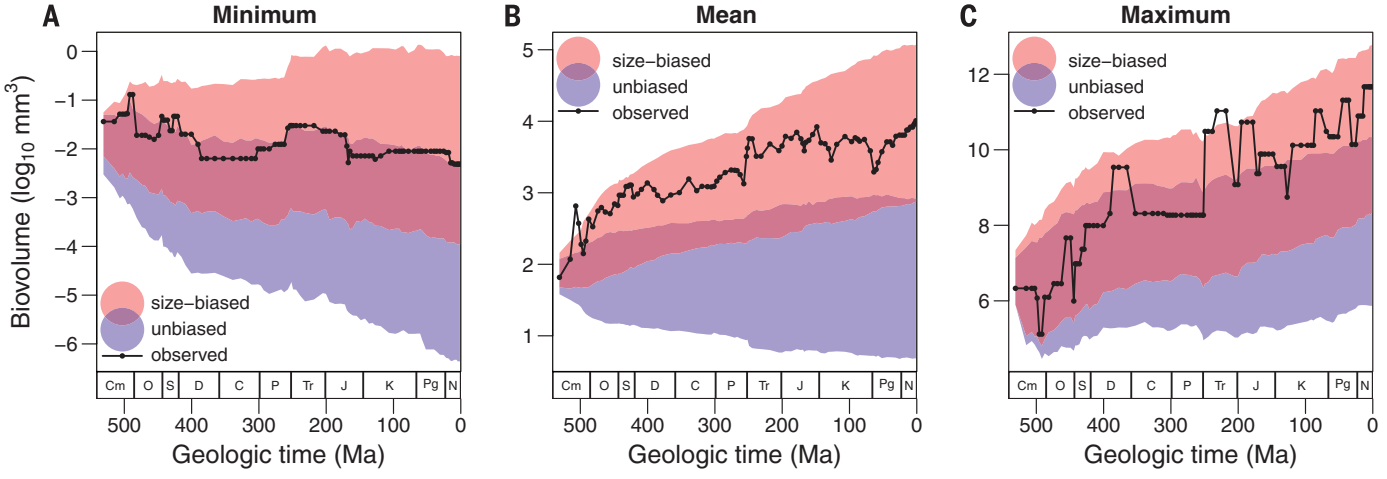

Fig. 2. Comparison of observed biovolume trends to those obtained from stochastic branching models (*23*). The colored regions highlight the size space occupied by 90% of the 1000 model runs. For clarity, only results for the size-biased (red) and unbiased (blue) models are shown; except below the minimum size, the lower-bounded model produced results nearly identical to the unbiased model (fig. S4). (**A**) Minimum, (**B**) mean, and (**C**) maximum sizes. Time scale abbreviations are the same as in Fig. 1.

but the observed mean and maximum sizes trended above the predicted range for the unbiased and lower-bounded models (Fig. 2 and fig. S4). As an additional test of the three models, we compared the observed distribution of biovolumes of all 2280 Pleistocene genera, the most recent and taxonomically diverse time interval in our analyses, to distributions predicted by our branching models and found strong support for the size-biased model over the other two models (table S2) (*23*). Finally, we used an independent, likelihood-based approach to compare support among five models for the trend in mean size over the entire 542 million years (*23*). Three models assumed a single mode of size evolution across the Phanerozoic (driven trend, random walk, or stasis). The best-supported of these models was the driven trend toward larger size (Table 1). However, allowing a shift in model type and parameters at the era-bounding mass extinctions improved the overall model fit, with the best-fit model in the Paleozoic being a driven trend toward larger size, followed by stasis in the Mesozoic, and a reversion to a driven trend in the Cenozoic (*23*) (Table 1). Removing the marine tetrapods, which tend to be very large, did not change this result (table S3). Thus, most of Phanerozoic time has been characterized by a trend toward larger animal sizes.

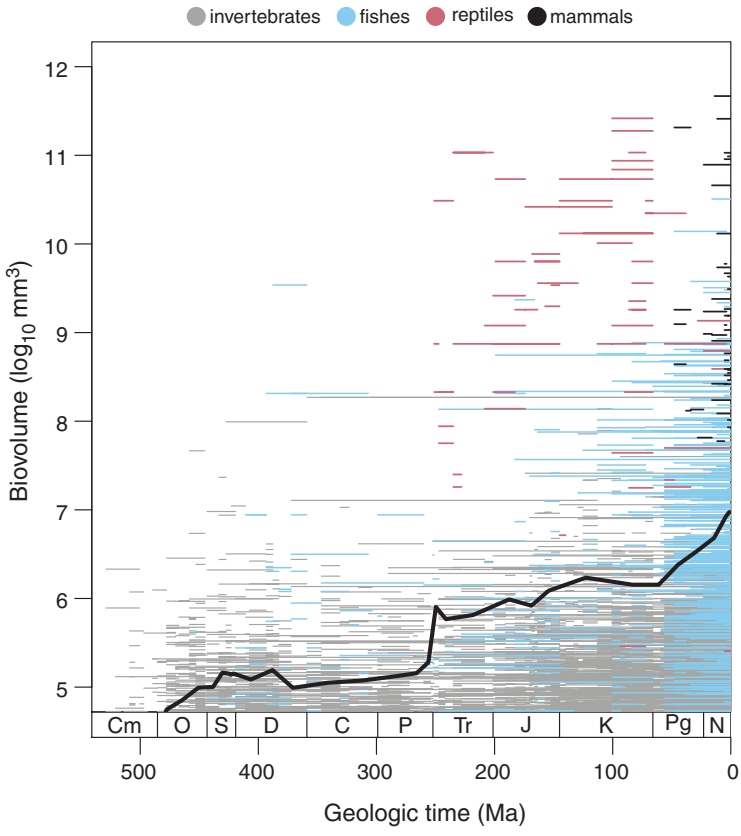

Fig. 3. Taxonomic compositions of the largest genera. Fishes and, later, air-breathing tetrapods, dominate the top of the size distribution. All genera with epoch- or stage-resolved stratigraphic ranges are plotted here, allowing for the inclusion of more large vertebrates. Horizontal lines show genus durations. The heavy black line demarcates the 95th percentile of all genera. Time scale abbreviations are the same as in Fig. 1.

The trends in minimum, mean, and maximum biovolume of marine animals are consistent with actively driven size increase and not consistent with simple neutral drift away from an initially small ancestor. To determine the extent to which this trend reflects size increase at low taxonomic levels across all phyla versus differential diversification of higher taxa with different mean sizes, we compared the observed trend in the mean to the expected trend if size were kept constant as diversity changed within different levels of the Linnaean hierarchy (fig. S5). This comparison demonstrates that much of the observed size increase reflects differential diversification among classes and is consistent with hierarchical size evolution in Paleozoic brachiopods (*15*). This finding also sheds light on the tripartite nature of the Phanerozoic trend in mean biovolume, as there was little differential diversification among classes during Mesozoic time (fig. S1B).

The dominance of differential diversification at the class level in producing the overall trend toward larger animal sizes emphasizes the hierarchical nature of evolutionary processes. In addition, it suggests that the widespread bias toward selection for larger size observed in extant populations (*8*) is unlikely to propagate into large-scale evolutionary trends observed in the fossil record. If the Phanerozoic trend reflected widespread selection for larger size at low taxonomic levels, we would expect to see most of the size trend explained by size increase within families, the lowest taxonomic level at which we can aggregate our data. These findings suggest that the factors favoring the overall trend toward larger size in marine animals relate to basic body plan and ecological life mode rather than competitive advantages associated with size differences within populations. These findings do not rule out an additional, smaller component related to widespread selection for larger size within populations, as there is also a component of size increase that occurs within families (fig. S5).

The taxonomic composition of the smallest and largest genera over time suggests the operation

Table 1. Results of model comparisons for the Phanerozoic trend in mean biovolume. Lower corrected Akaike information criterion (AICc) and higher Akaike weights indicate more support for a given model. logL is the log likelihood, and *K* is the number of free parameters in each model. The two-phase model has a break point at the Permian/Triassic boundary. The three-phase model has break points at the Permian/Triassic and Cretaceous/Paleogene boundaries. The best-fit model for each phase is used in multiphase models. The three-phase model is the best-supported model. See the supporting materials for details of the statistical methods (*23*). n/a, not applicable.

	logL	AICc	*K*	Akaike weight	Akaike weight single-phase model comparison
Random walk	53.7	-103.3	2	0.000	0.305
Driven trend	55.6	-104.9	3	0.000	0.695
Stasis	-63.7	131.5	2	0.000	0.000
Two-phase (driven trend/random walk)	60.5	-110.4	5	0.001	n/a
Three-phase (driven trend/stasis/driven trend)	71.2	-124.8	8	0.999	n/a

of constraints at the size extremes, even if these constraints are not required to model the overall distribution of animal sizes. The size minimum has been populated nearly exclusively by ostracods (a class of exclusively small-bodied crustaceans) since Silurian time (420 Ma). With the exception of the Middle/Late Triassic (235 Ma), where there is a maximum in ostracod size and a minimum in other animals, no other group in our data set comes within a factor of 6 of the smallest ostracod. The size maximum has been populated entirely by chordates since the Early Triassic (252 Ma), with no other genus since then coming within a factor of 2.5 of the largest chordate.

The dominance of a single phylum at each end of the size spectrum could result from simple incumbency effects, but transitions over time in the class affinities of the largest marine chordates suggest that physiology is also an important constraint, at least on the overall maximum size of marine animals. Nearly all of the largest solitary marine bilaterian genera have been reptiles and mammals. Tetrapods first reinvaded the oceans during Late Permian time (260 Ma) and rapidly occupied the size maximum (Fig. 3). Reptiles continued to dominate the top end of the size spectrum during the Mesozoic. Cetaceans were the first mammals to evolve a marine lifestyle and have occupied the largest marine body sizes since they first invaded the oceans during the Eocene (48 Ma) (Fig. 3). Air breathing is an exaptation (*25*) that can explain the rapid and widespread attainment of large size in marine reptiles and mammals. Relative to water, air has 20 to 30 times the concentration of O_2, is up to 100 times less viscous, has diffusion rates of O_2 through membranes that are 300,000 times faster, and is about 1000 times less dense (*26*). Thus, large animals are better able to meet their metabolic needs by breathing air than by breathing water. In fact, O_2 limitation has been proposed as a mechanism for limiting the evolutionary emergence of large, free-swimming, predatory bilateria generally (*27*, *28*).

Synoptic size data show that the average size of marine animals has increased substantially since the Cambrian and that this increase reflects differential diversification of large-bodied classes rather than neutral drift. A remaining question is the extent to which this differential diversification was enabled by intrinsic factors such as physiology, escalatory interactions between predators and prey (*29*), or changes in the physical and non-animal environment, such as oxygen availability (*30*) or the amount and quality of primary production (*7*). Testing among these controls will be critical to understanding how the physical and biological environments combine to shape the evolution of global ecosystems.

REFERENCES AND NOTES

1. R. H. Peters, *The Ecological Implications of Body Size* (Cambridge Univ. Press, Cambridge, 1983).
2. J. H. Brown, *Macroecology* (Univ. of Chicago Press, Chicago, 1995).
3. E. D. Cope, *Am. Nat.* **19**, 234–247 (1885).
4. E. D. Cope, *The Primary Factors of Organic Evolution* (Open Court, London, 1896).
5. C. J. J. Depéret, *The Transformations of the Animal World* (Paul, Trench, Trübner; London, 1909).
6. N. D. Newell, *Evolution* **3**, 103–124 (1949).
7. R. K. Bambach, *Paleobiology* **19**, 372–397 (1993).
8. J. G. Kingsolver, D. W. Pfennig, *Evolution* **58**, 1608–1612 (2004).
9. B. Rensch, *Evolution* **2**, 218–230 (1948).
10. J. Alroy, *Science* **280**, 731–734 (1998).
11. A. J. Arnold, D. C. Kelly, W. C. Parker, *J. Paleontol.* **69**, 203–210 (1995).
12. B. A. Maurer, *Evol. Ecol.* **12**, 925–934 (1998).
13. M. Laurin, *Syst. Biol.* **53**, 594–622 (2004).
14. D. W. E. Hone, T. M. Keesey, D. Pisani, A. Purvis, *J. Evol. Biol.* **18**, 587–595 (2005).
15. P. M. Novack-Gottshall, M. A. Lanier, *Proc. Natl. Acad. Sci. U.S.A.* **105**, 5430–5434 (2008).
16. D. Jablonski, *Nature* **385**, 250–252 (1997).
17. S. J. Gould, *J. Paleontol.* **62**, 319–329 (1988).
18. D. S. Moen, *J. Evol. Biol.* **19**, 1210–1221 (2006).
19. M. J. Monroe, F. Bokma, *J. Evol. Biol.* **23**, 2017–2021 (2010).
20. R. J. Butler, A. Goswami, *J. Evol. Biol.* **21**, 1673–1682 (2008).
21. J. H. Knouft, L. M. Page, *Am. Nat.* **161**, 413–421 (2003).
22. S. M. Stanley, *Evolution* **27**, 1–26 (1973).
23. Materials and methods are available as supplementary materials on *Science* Online.
24. J. J. Sepkoski Jr., *Bull. Am. Paleontol.* **363**, 1–500 (2002).
25. S. J. Gould, E. S. Vrba, *Paleobiology* **8**, 4–15 (1982).
26. D. Pauly, *Gasping Fish and Panting Squids: Oxygen, Temperature and the Growth of Water-Breathing Animals* (International Ecology Institute, Oldendorf, Germany, 2010).
27. T. W. Dahl *et al.*, *Proc. Natl. Acad. Sci. U.S.A.* **107**, 17911–17915 (2010).
28. E. A. Sperling *et al.*, *Proc. Natl. Acad. Sci. U.S.A.* **110**, 13446–13451 (2013).
29. G. J. Vermeij, *Annu. Rev. Ecol. Syst.* **25**, 219–236 (1994).
30. H. D. Holland, *Philos. Trans. R. Soc. London Ser. B* **361**, 903–915 (2006).

ACKNOWLEDGMENTS

We thank G. Griggs, M. Faerber, M. Laws, S. Sanghvi, L. Taylor, and the many undergraduate and high-school students for making body size measurements. J. Saltzman helped recruit high-school students. G. Hunt assisted with time series analysis. A. Clauset and M. A. Etnier kindly made their body size data on extant marine mammals available. Funding was provided by NSF grant EAR-1151022, the Stanford School of Earth Sciences, and the Swarthmore College James Michener Faculty Fellowship. Raw data files used for all analyses are permanently archived in the Stanford Digital Repository (http://purl.stanford.edu/rf761bx8302). This is Paleobiology Database publication 217.

SUPPLEMENTARY MATERIALS

www.sciencemag.org/content/347/6224/867/suppl/DC1
Materials and Methods
Figs. S1 to S6
Tables S1 to S3
Caption for Database S1
References (*31*–*120*)

18 August 2014; accepted 19 December 2014
10.1126/science.1260065

SPATIAL NAVIGATION

Disruption of the head direction cell network impairs the parahippocampal grid cell signal

Shawn S. Winter,* Benjamin J. Clark,*† Jeffrey S. Taube‡

Navigation depends on multiple neural systems that encode the moment-to-moment changes in an animal's direction and location in space. These include head direction (HD) cells representing the orientation of the head and grid cells that fire at multiple locations, forming a repeating hexagonal grid pattern. Computational models hypothesize that generation of the grid cell signal relies upon HD information that ascends to the hippocampal network via the anterior thalamic nuclei (ATN). We inactivated or lesioned the ATN and subsequently recorded single units in the entorhinal cortex and parasubiculum. ATN manipulation significantly disrupted grid and HD cell characteristics while sparing theta rhythmicity in these regions. These results indicate that the HD signal via the ATN is necessary for the generation and function of grid cell activity.

The ability to navigate is critical for survival of all animals and relies on a broad network of hippocampal and limbic brain circuits (*1*, *2*). The parahippocampal cortex contains grid cells, which fire at multiple locations, forming a hexagonal pattern covering the entire environment (*3*, *4*). Computational models explain grid cell generation from combined inputs of distance and direction displacement, which can subsequently be used for path integration (*5*–*7*). Theta rhythm is thought to be necessary for the computation of distance in grid cell models, and disruption of this signal eliminates gridlike firing patterns (*8*, *9*). HD cells fire as a function of an animal's directional orientation in the horizontal plane and are thought to convey the directional heading component to grid cells. However, some models use movement-direction cells, which have yet to be experimentally verified (*10*). The HD cell signal is generated subcortically and then projected rostrally via the anterior thalamic nuclei (ATN) to the parahippocampal cortices (*2*, *11*, *12*). Two nuclei within the ATN are known to contain HD cells—the anterodorsal and anteroventral thalamic nuclei (*13*, *14*). We tested the role of the HD signal in generating grid cell activity in the parahippocampal cortices.

Experiment 1 recorded from parahippocampal cortex, including medial entorhinal cortex (MEC) and parasubiculum, while female Long-Evans rats

Department of Psychological and Brain Sciences, Center for Cognitive Neuroscience, Dartmouth College, Hanover, NH 03755, USA.
*These authors contributed equally to this work. †Present address: Department of Psychology, University of New Mexico, Albuquerque, NM 87131, USA. ‡Corresponding author. E-mail: jeffrey.taube@dartmouth.edu